PAPER

Sustainable syngas generation from methane: enhanced catalysis with metal-promoted nickel on silica–alumina composites†

Ahmed S. Al-Fatesh, [ID] *[a] Ahmed A. Ibrahim,[a] Mohammed O. Bayazed,[a] Ahmed E. Abasaeed,[a] Maher M. Alrashed,[a] Mohammed F. Alotibi,*[b] Anis H. Fakeeha[a] and Ahmed I. Osman [ID] *[c]

To combat climate change and its association with emissions from fossil fuels, scientists are investigating sustainable substitutes. One promising approach is the dry reforming of methane, which turns greenhouse gases like CO_2 and CH_4 into lucrative syngas feedstock. However, catalyst optimization is necessary for effective dry reforming of methane. The optimum DRM conversion with perfect H_2 to CO ratio can only be achieved by stabilizing active sites "Ni" against high temperatures and increasing the interaction of CO_2 by using proper support and promoters. Investigating Ni catalysts on silica–alumina (SiAl) composites with promoters such as iridium (Ir), rhodium (Rh), ruthenium (Ru), platinum (Pt), and palladium (Pd) filled this research gap by modifying reducibility, basicity and crystallinity of the catalysts. The catalysts were analyzed by using different characterization approaches and optimized for the dry reforming of methane using a central composite design. The objectives were to determine the best promoter, optimize the procedure for maximum conversion rates and the optimal composition of syngas, and assess the catalytic characteristics. According to the results, Rh-promoted Ni catalysts performed the best, converting 93.1% of CO_2 and 87.0% of CH_4 under optimum circumstances, with an optimal H_2/CO ratio of 0.99 for syngas. The NiRh/SiAl outperforms others due to the extraordinary degree of reduction and higher side of reducibility of NiO which undergoes moderate interaction with the support.

[a]*Chemical Engineering Department, College of Engineering, King Saud University, P.O. Box 800, Riyadh 11421, Saudi Arabia. E-mail: aalfaesh@ksu.edu.sa*

[b]*Institute of Refining and Petrochemicals Technologies, King Abdulaziz City for Science and Technology (KACST), P.O. Box 60, Saudi Arabia. E-mail: mfalotaibi@kacst.gov.sa*

[c]*School of Chemistry and Chemical Engineering, Queen's University Belfast, Northern Ireland, Belfast, UK. E-mail: aosmanahmed01@qub.ac.uk*
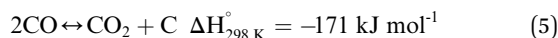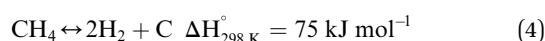
† Electronic supplementary information (ESI) available: paragraph S1: Selection of 1 wt% promoter loading S1; S2: Catalyst characterization; paragraph; Fig. S1: SEM of the fresh NiRh/SiAl catalyst; Fig. S2: Composition of the NiRh/SiAl catalyst as per EDX analysis; Table S1: Various % average conversion; Table S2: Compares the findings of this study with those previously published. See DOI: https://doi.org/10.1039/d4se00529e.

1. Introduction

Seasonal changes, extreme weather, and rising sea levels are all results of global warming, which is caused by an increase in greenhouse gases like carbon dioxide and methane from the burning of fossil fuels in industry.[1,2] Even if renewable energy innovations are encouraging, fossil fuels continue to be widely used. This calls for the quick development of effective strategies to reduce emissions and lessen the growing effects of global warming on the environment.[1–3]

In this scenario, the conversion of methane (CH_4) and carbon dioxide (CO_2) into syngas, which is a mixture of hydrogen (H_2) and carbon monoxide (CO), has shown great potential as a method for utilizing greenhouse gases as resources and reducing their negative impact on the environment.[4] Syngas is a valuable chemical feedstock used in a variety of applications. Among various methods, the dry reforming of methane (DRM) has emerged as a promising approach for significantly reducing both CH_4 and CO_2 emissions.[5–7] Steam reforming of natural gas, which yields grey hydrogen, is the most popular industrial method for producing syngas,[8–10] as shown in eqn (1). The steam reforming process has two major problems: firstly, high emission of CO_2, which reduces the system energy efficiency by 6–10% when the CO_2 capture process is involved, and secondly because the H_2 purity in the reformer gas is not high, additional operations such as purification, separation, and compression are required to achieve high purity of H_2. This further incurs additional energy penalties. Nevertheless, steam reforming is the widely used method to create a hydrogen-rich synthesis gas. Despite higher energy consumption, the beauty of the DRM reaction is the consumption of two greenhouse gases, CH_4 & CO_2, making it more environmentally conscious than other reforming

reactions (eqn (2)). So, it bears more interest in the production of synthetic fuel than steam reforming;[11,12] it involves the reaction of methane with CO_2 to produce syngas, as shown in eqn (2).

$$CH_4 + H_2O \leftrightarrow 3H_2 + CO \quad \Delta H^{\circ}_{298\,K} = 206 \text{ kJ mol}^{-1} \quad (1)$$

$$CH_4 + CO_2 \leftrightarrow 2H_2 + 2CO \quad \Delta H^{\circ}_{298\,K} = 247 \text{ kJ mol}^{-1} \quad (2)$$

The DRM process not only utilizes two major greenhouse gases but also presents a solution for managing low-value streams like landfill gases.[13] The implementation of DRM technology is facing certain challenges. The process requires a substantial amount of energy input, making it highly endothermic. In addition, it is crucial to develop catalysts that can remain active and stable at lower operating temperatures (approximately 650–750 °C).[14] The catalysts that are to be developed must also be resistant to deactivation mechanisms such as sintering and coke formation, which can reduce their efficiency significantly over time.[15,16]

$$H_2 + CO_2 \leftrightarrow H_2O + CO \quad \Delta H^{\circ}_{298\,K} = 41 \text{ kJ mol}^{-1} \quad (3)$$

$$CH_4 \leftrightarrow 2H_2 + C \quad \Delta H^{\circ}_{298\,K} = 75 \text{ kJ mol}^{-1} \quad (4)$$

$$2CO \leftrightarrow CO_2 + C \quad \Delta H^{\circ}_{298\,K} = -171 \text{ kJ mol}^{-1} \quad (5)$$

Eqn (3)–(5) represent the side reactions that are commonly observed during the operation of DRM, and they reduce its activity and stability. Therefore, the main challenges that need to be addressed for efficient operation include catalyst deactivation due to coking and competition from the reverse water gas shift reaction. DRM is a potential technique for cutting greenhouse gas emissions, and researchers are working to overcome weaknesses in the current catalysts. By investigating innovative nickel-based catalysts supported on silica–alumina composites, this study seeks to contribute. The goal is to find the best promoter—a noble metal such as palladium, ruthenium, platinum, iridium, or rhodium—that can increase the rates at which carbon dioxide (CO_2) and methane (CH_4) are converted in DRM at the same time.[17] Our catalysts' efficiency will be evaluated at a reaction temperature of 700 °C, a space velocity of 42 000 ml h^{-1} g_{cat}^{-1}, and a reaction time of 420 minutes.[18,19] The selection of these promoters is grounded in their known impacts on catalyst activity and stability, which are crucial for the DRM reaction's overall efficiency.[20] By doing so, we hope to address the existing challenges with catalyst performance in DRM and develop more effective catalysts.

2. Experimental

2.1 Materials used

The experiment used commercially available silica–alumina with a 2 : 1 SiO_2/Al_2O_3 ratio as the support material and ultrapure water from a Milli-Q system as the solvent. The metal precursors, including palladium nitrate dihydrate, ruthenium

nitrate hexahydrate, rhodium nitrate hexahydrate, iridium nitrate, platinum nitrate, and nickel nitrate hexahydrate, were all purchased from Alfa Aesar and used without further purification.

2.2 Catalyst preparation

A series of nickel catalysts were synthesized using the wet impregnation method. Nickel nitrate hexahydrate (5 wt% loading) was the main active metal precursor, with promoters (palladium, platinum, iridium, ruthenium, or rhodium nitrate precursors) each at 1 wt% loading. All precursors were dissolved in stoichiometric quantities in 20 ml of ultrapure water and stirred magnetically for two hours at 80 °C to ensure complete dissolution and even dispersion on the support. The resultant slurry was dried overnight at 120 °C to remove excess water and solvents and then calcined at 800 °C for three hours to create stable, active catalyst sites. The calcined material was crushed into a powder and denoted as Ni + x/SiAl (x = Pd, Pt, Ir, Ru, Rh), where "x" denotes the specific promoter type. Section S1 in the ESI† provides a detailed justification for the 1 wt% promoter loading.

2.3 Catalyst performance evaluation

2.3.1 DRM reaction experiments. The DRM tests were conducted at atmospheric pressure in a fixed-bed stainless-steel reactor, measuring 30 cm in length and 9.1 mm in diameter. The reactor was packed with quartz wool to support a precisely weighed catalyst bed (0.1 g), ensuring consistent contact between reactants and the catalyst. The reaction temperature was monitored using a K-type thermocouple placed inside the catalyst bed.

Prior to the reaction, the catalyst was reduced by flowing hydrogen gas (40 ml min^{-1}) at 800 °C for 60 minutes. Post-reduction, any remaining hydrogen was purged by adjusting the reactor temperature to the desired reaction temperature (e.g., 700 °C) while maintaining a nitrogen flow rate of 15 ml min^{-1} for 30 minutes.

The DRM reaction commenced by introducing a feed mixture of methane, carbon dioxide, and nitrogen in a 3 : 3 : 1 ratio at a total flow rate of 70 ml min^{-1}, corresponding to an hourly space velocity of 42 000 ml (h^{-1} g_{cat}^{-1}). The conversions of methane (CH_4) and carbon dioxide (CO_2), as well as the hydrogen-to-carbon monoxide (H_2/CO) ratio, were continuously monitored using an online gas chromatograph equipped with a thermal conductivity detector (TCD). This setup enabled precise and real-time analysis of the reactor outlet stream composition, providing accurate performance metrics for the catalysts under study.

$$X_{CH_4}\% = \frac{[CH_{4,in}] - [CH_{4,out}]}{[CH_{4,in}]} \times 100 \quad (6)$$

$$X_{CO_2}\% = \frac{[CO_{2,in}] - [CO_{2,out}]}{[CO_{2,in}]} \times 100 \quad (7)$$

$$\text{Hydrogen carbon monoxide ratio} = \frac{[H_2]}{[CO]} \quad (8)$$

where [CH$_{4,\ in}$] represents the initial methane in the feed, [CH$_{4,\ out}$] is the methane output, and [H$_2$] and [CO] are the products after the reaction.

2.3.2 Experimental design and process optimization

2.3.2.1 Central composite design. Central composite design (CCD) offers a powerful approach to optimizing reforming processes by strategically selecting key variables such as temperature, feed ratio, and catalyst concentration. CCD involves three types of experiments: central points representing average values, axial points exploring high and low extremes, and star points pushing the boundaries even further. This comprehensive data collection allows researchers to build a mathematical model that captures not just the individual effects of these factors but also their complex interactions.

This model goes beyond merely summarizing data; it enables the prediction of reforming outcomes under various conditions. Notably, CCD achieves this with fewer experiments compared to traditional methods, making it a highly efficient approach. Ultimately, CCD empowers researchers to optimize the reforming process while gaining a deeper understanding of the intricate interplay between variables that govern the entire process.

The studied experimental factors comprise the space velocity, temperature, and CH$_4$/CO$_2$ molar ratio. Each of them has a lower limit of $x_{i\ min}$ and an upper limit of $x_{i\ max}$. The mean value of x_i over the interval $[x_{i\ min}, x_{i\ max}]$ is termed the center of the interval in eqn (9)

$$\bar{X}_{oi} = (x_{i\ max} + x_{i\ min})/2 \qquad (9)$$

And the deviation of either limit from the mean is described in eqn (10)

$$\Delta x_i = x_{i\ max} - x_{i\ min}/2 \qquad (10)$$

In experimental design, the point with coordinates ($\bar{X}_{o1}$, $\bar{X}_{o2}$, $\bar{X}_{o3}$, ..., $\bar{X}_{on}$) is called the center point of the design, which is a specific combination of the input variables that are typically included to allow for the detection of curvature in the response surface. These values are changed to code dimensionless variables X_i in the range of +1 and −1 using the following transformation in eqn (11)

$$X_i = \frac{x_i - \bar{X}_{oi}}{\Delta x_i} \qquad (11)$$

where x_i is the original value of the ith input variable, and Δx_i is the range of values for that variable.

In experimental design, the response of a system is often modeled as a function of the factors using a polynomial equation. The Taylor Series expansion can be used to derive this polynomial equation by approximating the response surface as a series of linear and quadratic terms or sometimes of third order.[21] In our case, the full quadratic model with three factors, as shown in eqn (12), is preferable.

$$Y = \beta_0 + \sum_{i=1}^{3} \beta_i X_i + \sum_{i=1}^{2} \sum_{j=i+1}^{3} \beta_{ij} X_i X_j + \sum_{i=1}^{3} \beta_{ii} X_i^2 + \varepsilon \qquad (12)$$

where Y is the response variable, X_1, X_2, and X_3 are the input coded or actual values of the factors that affect the response variable, β_0, β_i, β_{ij} and β_{ii}, $i, j = 1, 2, 3$ are the regression coefficients of intercept, linear, interaction, and quadratic terms, and ε is the error term, which represents the random variation that is not explained by the independent variables.[22]

2.3.2.2 Process optimization. The process optimization was done by maximizing the response variables (CH$_4$ conversion, CO$_2$ conversion, and the H$_2$/CO ratio) and using design experiment version 13, which has the optimization goals, so it gives many solutions that fit the required goals and selected the optimum conditions based on the solution with the highest desirability value. The ESI section contains details of the characterization (S2)† of the catalyst, aligning with the content presented in our paper (referenced).

3. Results

3.1 Catalyst textural properties

N$_2$ adsorption–desorption isotherms show that all of the Ni + x/SiAl catalysts (where x = Ir, Pd, Pt, Rh, Ru) have a consistent mesoporous structure. Both the type IV isotherm and H1 hysteresis loop shown in Fig. 1 demonstrate this. The reversible adsorption and desorption curves show a narrow distribution of mesopores, and pores are free from the percolation effect. A similar type of pore size distribution profile of all catalysts shows homogeneity in pore distribution (Fig. 1b). Table 1 provides consistent values for all catalysts in terms of surface area (314–345 m^2 g^{-1}), pore volume (0.50–0.53 cm^3 g^{-1}), and pore diameter (6.3–6.5 nm). The narrow distribution of pores over high surface area samples shows the consistent flow of gas feed in the pore channels, adequately accessible active sites, and plenty of room for the interaction of reactants (CH$_4$ & CO$_2$) with the catalyst's active sites. These features imply that these catalysts have the potential for successful methane dry reforming.

3.2 H$_2$-TPR and CO$_2$-TPD analysis

H2-temperature programmed reduction (TPR) determines the ease with which a catalyst is reduced by hydrogen against temperature, revealing the degree of nickel (Ni) dispersion on the support material. Promoters can lower the Ni reduction temperature, potentially increasing activity during DRM. The number of peaks and their locations in H2-TPR profiles indicate different levels of interaction between Ni and the support.[23] For instance, Ru-promoted and Ir-promoted catalysts show a low-temperature reduction peak for RuO$_2$ at 150 °C and a reduction peak for IrO$_2$ at 250 °C.[21,24,25] Interestingly, all catalysts show reduction peaks in the intermediate temperature region (400–650 °C) and high-temperature region (700–900 °C). The former reflects the amount of H$_2$ needed to reduce moderately interacting NiO, while the latter reflects the amount needed for strongly interacting NiO. Notably, the Rh-promoted catalyst shows a shift towards lower temperatures in the intermediate region, indicating higher reducibility. Rhodium dissociates H$_2$ molecules into atomic hydrogen, which further reduces NiO at lower temperatures.[26,27]
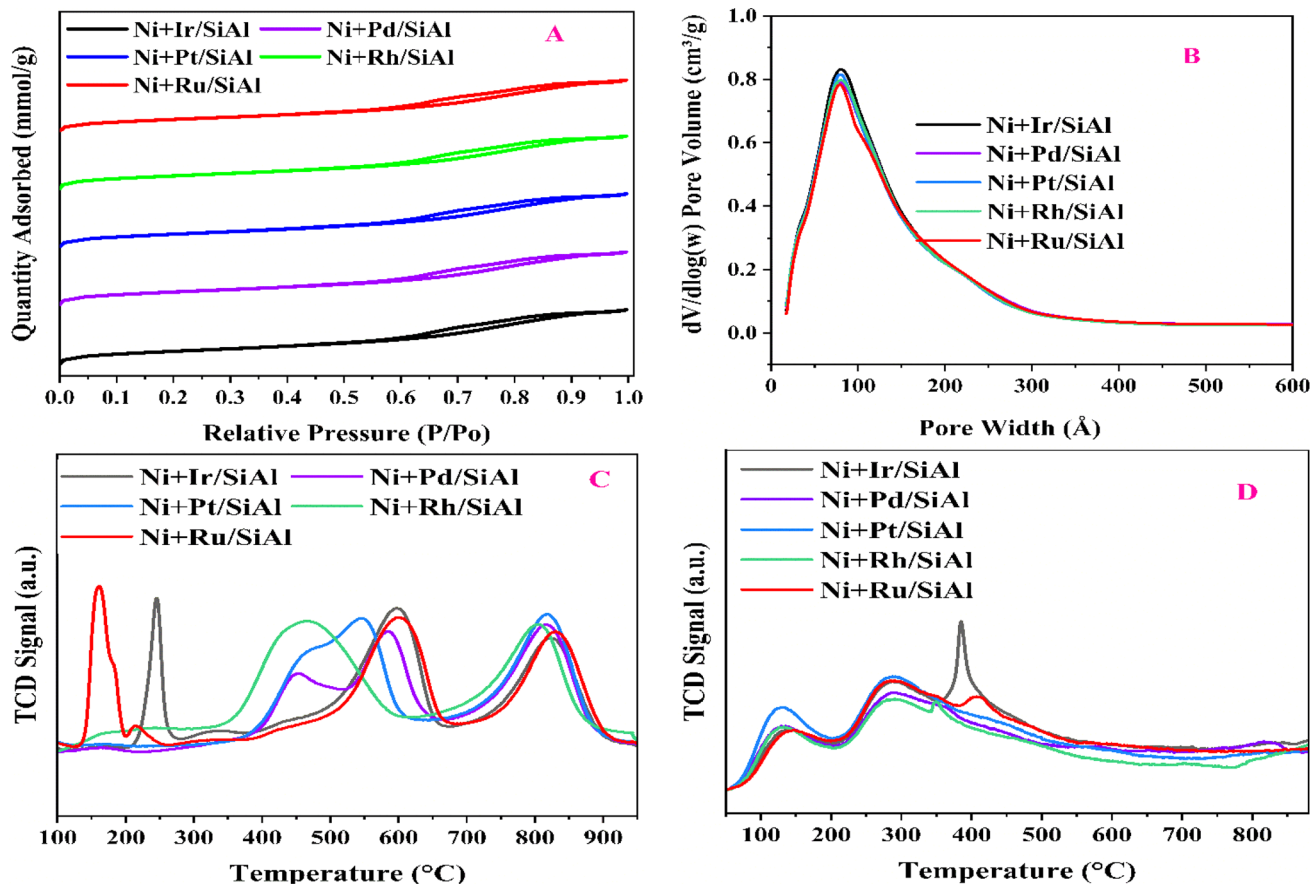
Fig. 1 (A) N_2 adsorption−desorption isotherms and (B) BJH distribution of the catalyst samples; (C) H_2-TPR (D) CO_2-TPD of the catalysts.

Table 1 The textural aspect of the catalysts

Catalyst	Abbreviated sample	BET-surface area (m^2 g^{-1})	Pore-volume (m^3 g^{-1})	Pore-size (nm)
5% Ni + 1% Ir/62.7% SiO_2 + 31.3% Al_2O_3	NiIr/SiAl	341	0.53	6.4
5% Ni + 1% Pd/62.7% SiO_2 + 31.3% Al_2O_3	NiPd/SiAl	335	0.52	6.3
5% Ni + 1% Pt/62.7% SiO_2 + 31.3% Al_2O_3	NiPt/SiAl	345	0.52	6.3
5% Ni + 1% Rh/62.7% SiO_2 + 31.3% Al_2O_3	NiRh/SiAl	338	0.52	6.3
5% Ni + 1% Ru/62.7% SiO_2 + 31.3% Al_2O_3	NiRu/SiAl	314	0.50	6.5

Data from TPR analysis, such as those that may be seen in Table 2 (reduction percentage, hydrogen consumption, and turnover frequency), aid in the comparison of catalyst performance and the understanding of how promoters affect Ni dispersion for enhanced dry reforming activity. The degree of reduction is found to be maximum over the Rh-promoted catalyst.

Temperature-Programmed Desorption (TPD) analysis looks at the strength of CO_2 molecules' binding to the catalyst surface. Weaker CO_2-catalyst bonds are indicated by lower desorption temperatures, which is advantageous for dry reforming. Because of the weaker binding, CO_2 may activate more easily, which encourages syngas formation. The CO_2-desorption profile shows the extent of interaction of CO_2 with the catalyst surface against temperature. While the release at intermediate temperatures (200–450 °C) supports medium-strength sites (perhaps surface oxygen anions), the observed diffuse CO_2 release at low temperatures (100–150 °C) suggests weak binding sites (presumably hydroxyl groups).[23,28] The earlier one is said to be medium strength basic sites, whereas the latter one is weak strength basic sites. A captivating correlation between activity and surface characteristics was found by analyzing the catalysts. With a dominating peak in the intermediate temperature range, the Ir-promoted catalyst indicates a significant concentration of medium-strength basic sites, which may be impeding its overall activity. On the other hand, the remaining catalysts have roughly a similar basicity pattern.

3.3 Catalytic activity

Before evaluating the catalysts, a catalytic performance test was conducted using an empty stainless-steel reactor at a reaction

Table 2 Hydrogen consumption during the TPR analysis

Sample	T (°C)	Quantity (cm^3 g^{-1} STP)	Total H$_2$ consumption from the TPR (cm^3 g^{-1} STP)	Degree of reduction[a] (%)	TOF[b] (h^{-1})
NiIr/SiAl	245.6	1.569	16.497	86.399	91.6
	328.4	0.049			
	337.7	0.105			
	598.9	8.529			
	824.1804	6.425			
NiPd/SiAl	448.1	1.428	16.520	86.519	93.0
	584.0	7.416			
	669.0	0.029			
	816.2	7.795			
NiPt/SiAl	546.6	10.093	18.981	99.408	101.0
	644.7	0.035			
	817.5	8.853			
NiRh/SiAl	239.2	0.131	19.752	103.446	153.0
	250.3	0.133			
	289.0	0.020			
	466.5	10.809			
	622.6	0.031			
	805.3	8.494			
	942.7	0.134			
NiRu/SiAl	160.2	2.856	18.272	95.699	107.0
	214.9	0.089			
	600.1	8.382			
	689.7	0.024			
	831.1	6.921			

[a] Degree of reduction (%) = (H$_2$ consumption during H$_2$-TPR/theoretical H$_2$ required to complete the reduction 19.094 cm^3 g^{-1} STP). [b] TOF = turnover frequency (h^{-1}).

temperature of 700 °C, maintaining a comparable feed ratio. The reported conversions of CO_2 (0.2%) and CH_4 (1.6%) from this test indicate that the metallic reactor had a negligible contribution to the reactions. Fig. 2A and B illustrate the CH_4 and CO_2 conversions achieved with the different catalysts. Among the catalysts, the NiRh/SiAl sample exhibited the highest average CH_4 conversion, reaching approximately 65.2%. The NiRh/SiAl catalyst also demonstrated the highest CO_2 average conversion, reaching about 71.5%. In contrast, the NiRu/SiAl, NiPt/SiAl, NiPd/SiAl, and NiIr/SiAl catalysts achieved lower CH_4 and CO_2 average conversions, with values ranging from 38.8% to 46.3% for CH_4 and 43.7% to 57.5% for CO_2. Notably, the NiPd/SiAl and NiIr/SiAl catalysts displayed the lowest activity performance. It's worth highlighting that the CO_2 conversion values exceeded the corresponding CH_4 conversions in all catalyst samples, possibly influenced by the reverse water gas shift's side reaction, which consumed generated H$_2$ (as shown in eqn (3)).[23] The data presented in Table 2 further emphasize the superior activity of the Rh-promoted catalyst. This is verified by its highest degree of reduction (103%) and the highest turnover frequency (153), indicating its exceptional catalytic performance. According to Table 2, the NiRh/SiAl catalyst showed the best reduction degree (103%) among all the catalysts, indicating that it had a better ability to convert metal oxides into active sites (Ni and Rh) compared to the other catalysts. This was further confirmed by the TEM images of the fresh NiRh/SiAl catalyst (Fig. 3C), which showed a well-dispersed honeycomb-like structure with a uniform

distribution of Ni and Rh metals throughout the support. This suggests that Rh could have promoted the reduction process, leading to the creation of more well-dispersed active sites for methane conversion. Table S1† displays the various % average conversion of the investigated catalysts in this work operated at 700 °C. Table S2† compares the findings of this study with those previously published for Ni-based catalyst systems promoted by noble and non-noble metals.

3.4 TGA and DTG

The assessment of carbon deposition was carried out through thermogravimetric analysis (TGA). Fig. 2C and D provide insights into the weight loss of carbon deposits on the catalyst samples and their derivatives. Fig. 2C illustrates the proportion of total weight loss, with the NiPd/SiAl catalyst exhibiting the highest weight loss at 41.2%. It was followed by the NiPt/SiAl, NiIr/SiAl, NiRu/SiAl, and NiRh/SiAl catalysts, which displayed weight losses of 11.2%, 9.9%, 8.9%, and 5.0%, respectively, under reaction conditions of 700 °C for 5 hours. Notably, the weight loss of carbon deposited on the NiRh/SiAl catalyst aligned well with its high catalytic activity. Fig. 2D presents the derivative of TGA (DTG), with the observed peak around 400 °C attributed to the oxidation of easily gasifiable amorphous carbon, as indicated in the literature.[23] Carbon nanotube (CNT)-type coke, which is more challenging to gasify, exhibited a peak around 500 °C, while the most challenging-to-gasify graphite-like coke displayed a peak above 600 °C. The DTG profiles of the catalysts revealed the presence of graphite-like coke, with
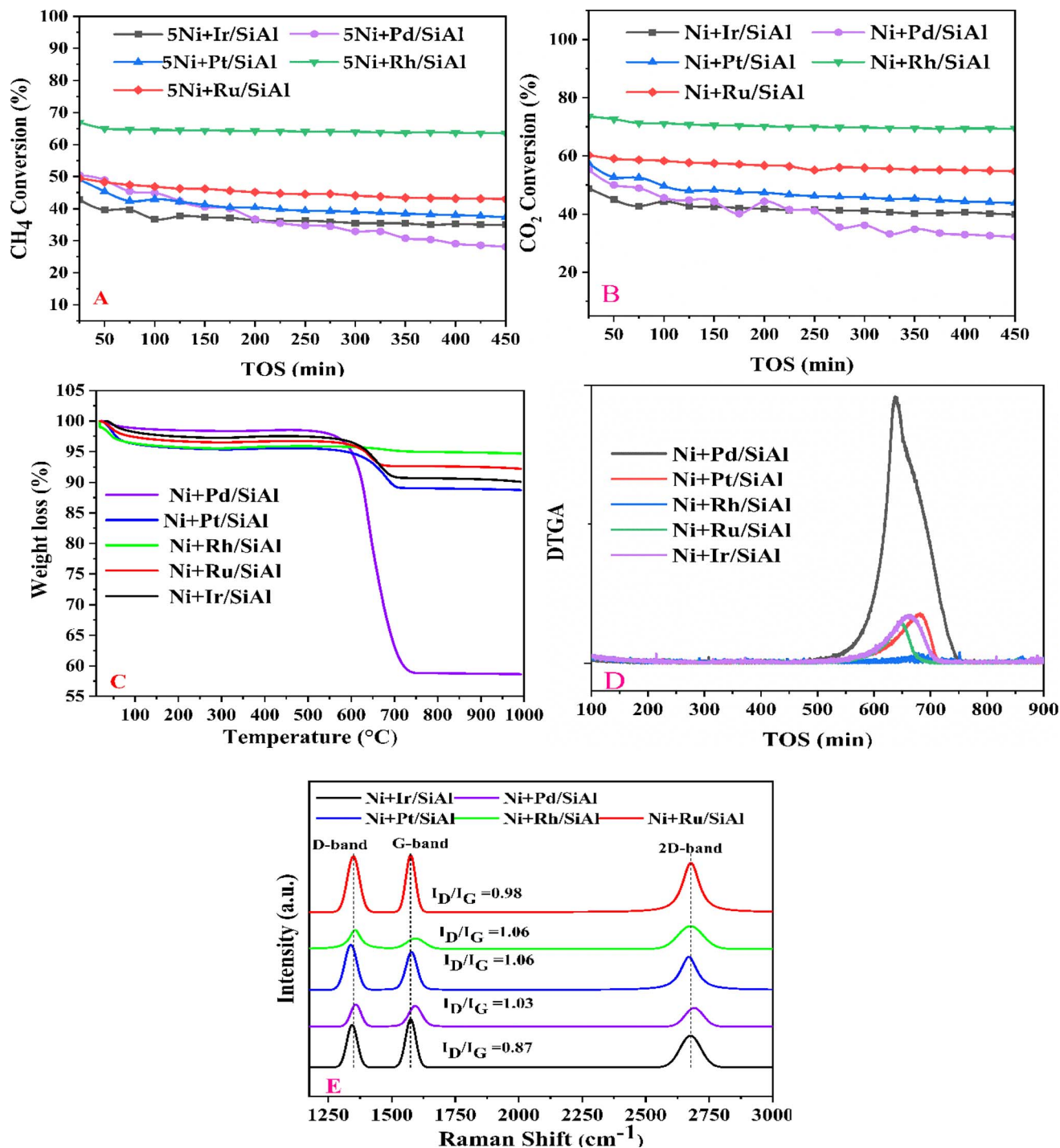
Fig. 2 Catalytic activity results: (A) CH_4 conversion (%) and (B) CO_2 conversion (%) vs. time on stream performed at 700 °C and GHSV of 30 000 ml h^{-1} g$_{cat}$$^{-1}$; (C) thermo-gravimetric analysis (D) derivative (DTG) of spent catalysts over five hours in the time on stream test; (E) Raman spectra of the used catalysts.

maximum peaks observed at temperatures of 637 °C, 643 °C, 644 °C, 676 °C, and 682 °C for NiPd/SiAl, NiRu/SiAl, NiIr/SiAl, NiRh/SiAl, and NiPt/SiAl, respectively.

Interestingly, the least active catalyst, NiPd/SiAl, exhibited the highest peak intensity, while the most active catalyst, NiRh/SiAl, displayed the lowest peak intensity. The effective functioning of a catalyst depends on the minimization of carbon deposition on its surface. If carbon deposition is kept in check, more active sites remain accessible on the catalyst surface, allowing it to adsorb and activate methane molecules, which leads to sustained conversion efficiency. However, if there is excessive carbon deposition, it can create a physical barrier that hinders the diffusion of reactant molecules CH_4 towards the active sites within the catalyst pores. This limitation reduces the
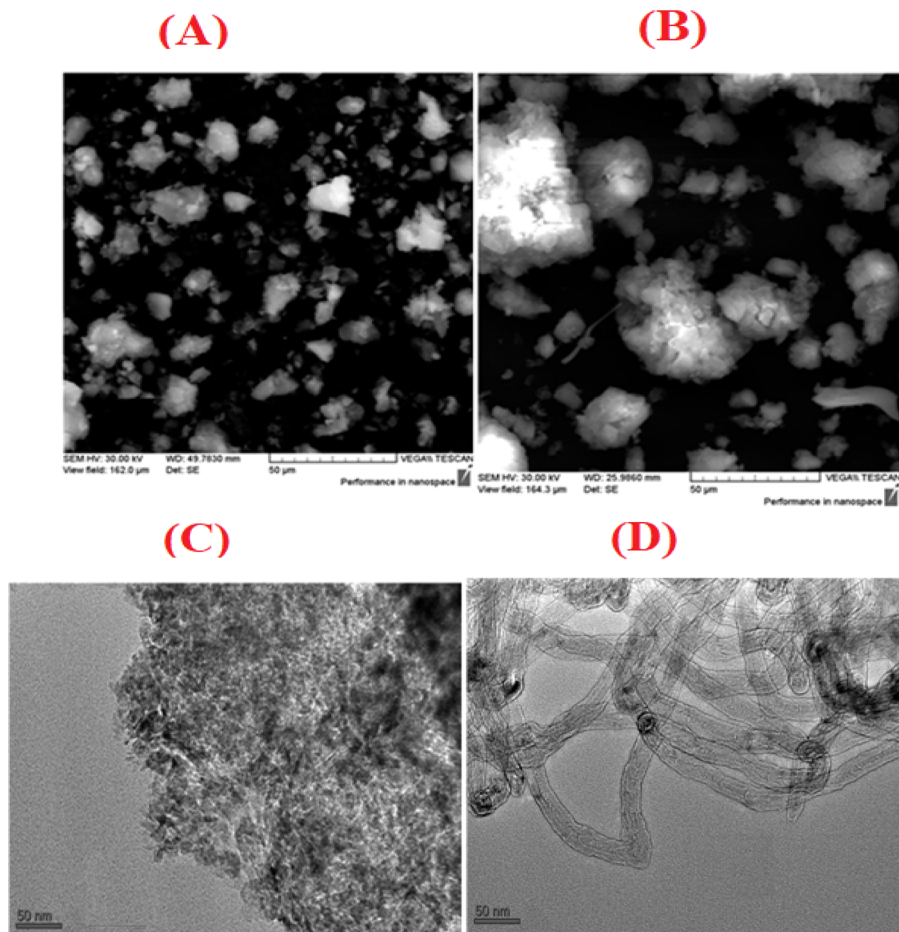
Fig. 3 SEM images of (A) fresh and (B) used NiRh/SiAl catalysts; TEM images of (C) fresh and (D) used NiRh/SiAl catalysts.

overall reaction rate, which ultimately affects long-term performance. Carbon accumulation can also act as an insulator, negatively impacting the transfer of heat within the catalyst, causing uneven temperature distribution, and potentially creating hotspots. In dry reforming of CH_4, such hotspots can trigger undesirable side reactions or even damage the catalyst structure, compromising long-term operation. The type of coke that accumulates on a catalyst surface can significantly affect its deactivation severity. Amorphous carbon is a less stable form of carbon that is easier to remove through high-temperature treatments, and the catalyst is less prone to forming it during long-term operation. As a result, it requires less frequent regeneration cycles, and the catalyst's performance is better sustained. Graphitic coke, on the other hand, is a highly stable but more detrimental form of carbon that is difficult to remove and can permanently block active sites, leading to a significant and irreversible loss of catalytic activity. The analysis shows that catalysts that mainly form graphitic coke experience a steeper decline in performance over time. Additionally, the structure of carbon nanotubes can also form during methane conversion, which can physically block active sites and hinder mass transfer, although it is less common than other types of coke. By controlling the type of coke formed and minimizing carbon deposition, catalysts can maintain their activity for a long time,

making them more efficient for methane conversion applications.

3.5 Raman spectroscopy analysis

The type and level of graphitization of carbon deposits on spent catalysts were examined using Raman spectroscopy. The typical peaks for each catalyst are displayed in Fig. 2E: the G band, approximately at 1576 cm^{-1}, suggests graphitic structures, whereas the D band, around 1350 cm^{-1}, indicates disordered carbon. The presence of graphitic carbon is further confirmed by the 2D band, which appears only in graphite.[29,30]

The degree of graphitization is quantified by the ratio (I_D/I_G) of the intensities of the D and G bands. Remarkably, the Ni + Ir/SiAl samples exhibit a lower I_D/I_G ratio compared to other catalysts with similar ratios around 1, indicating less disordered and possibly more graphitized carbon. This suggests that the Ni + Ir/SiAl catalyst may possess better structural integrity and stability due to the higher level of graphitization of the carbon deposits.

3.6 SEM analysis

SEM analysis results, displayed in Fig. 3A and B, feature both fresh and used NiRh/SiAl catalysts. The SEM images reveal the

presence of bright spots of varying sizes and shapes, representing the Ni and Rh particles. These particles primarily exhibit irregular shapes with some smooth surfaces, while the support material appears black in the images. The SEM image of the fresh catalyst showcases a well-distributed active metal surface. However, the image of the used catalyst displays sintered particles resulting from the reaction. The ESI† section includes a re-evaluation of the scanning electron microscopy (SEM) analysis of the fresh NiRh/SiAl catalyst. This analysis incorporates energy-dispersive X-ray spectroscopy (EDX) to determine the composition. Fig. S1 and S2 in the ESI† section present the results of SEM and EDX, respectively. The EDX composition results serve to validate and closely align with the intended design values for the catalyst preparation.

3.7 TEM analysis

Transmission electron microscopy (TEM) analysis reveals significant differences between the fresh and spent NiRh/SiAl catalysts. The fresh NiRh/SiAl catalyst displays a uniform and dispersed structure, while the spent NiRh/SiAl catalyst is populated with carbon nanotubes (CNTs), with the widths of the nanotubes being relatively uniform. The metal particles are spherical and uniformly sized.

For the used catalyst, the TEM observations are consistent with the results from TGA and Raman spectroscopy, which identify the carbon deposition resulting from the catalyst's activity in converting methane into carbon-based compounds. A higher degree of carbon deposition, as determined by these methods, correlates with a greater number of visible CNTs in the TEM images, indicating a higher conversion of methane into nanotubes. This highlights the catalyst's effectiveness and the extent of its carbon deposition during the DRM process.

3.8 Effect of reaction temperature

Fig. 4 shows how endothermic processes should behave, with CH_4 and CO_2 conversions increasing as temperature increases. The Arrhenius equation (eqn (13) and (14)) describes this

relationship among the temperature (T), rate constant (k), and activation energy (E). The rate constant (k) is proportional to the rate of consumption of CH_4 or the rate of consumption of CO_2. When the rate of consumption of CH_4 or rate of consumption of CO_2 is expressed equivalently by rate constant (k), activation energy is called apparent activation energy (E_a) and the Arrhenius equation is represented as follows:

$$k = A e^{\frac{-E_a}{RT}} \tag{13}$$

where A is the pre-exponential factor and R is the universal gas constant.

Eqn (14) is obtained by taking the logarithm of eqn (13) as follows:

$$\mathrm{Ln}(k) = \ln(A) - \frac{E_a}{RT} \tag{14}$$

After measuring the rate constant at various temperatures, a straight line is obtained by plotting $\ln(k)$ *versus* $1/T$. As is shown in eqn (14), the slope represents $-E_a/R$, and the intercept stands for the ln of the pre-exponential factor (A). R is the universal gas constant ($R = 8.314$ J mol^{-1}). In Table 3, the feed (CH_4 and CO_2) conversions for different reaction temperatures are presented.

The linear fit in Fig. 4B can be resolved to yield the Arrhenius equation parameters, and Table 4 shows the calculated parameters of the Arrhenius equation.

3.9 Predictive analysis and process optimization

The robustness of data fitting is examined by analysis of variance (ANOVA).[31] Table 5 lists the actual values of the studied factors.

3.9.1 Process modelling and analysis of variance. Introducing the transformation of response variables serves as a technique to stabilize response variance, normalize the distribution of the response variable, and enhance the model's data fitting. The Central Composite Design (CCD) method was used to identify a suitable power transformation for
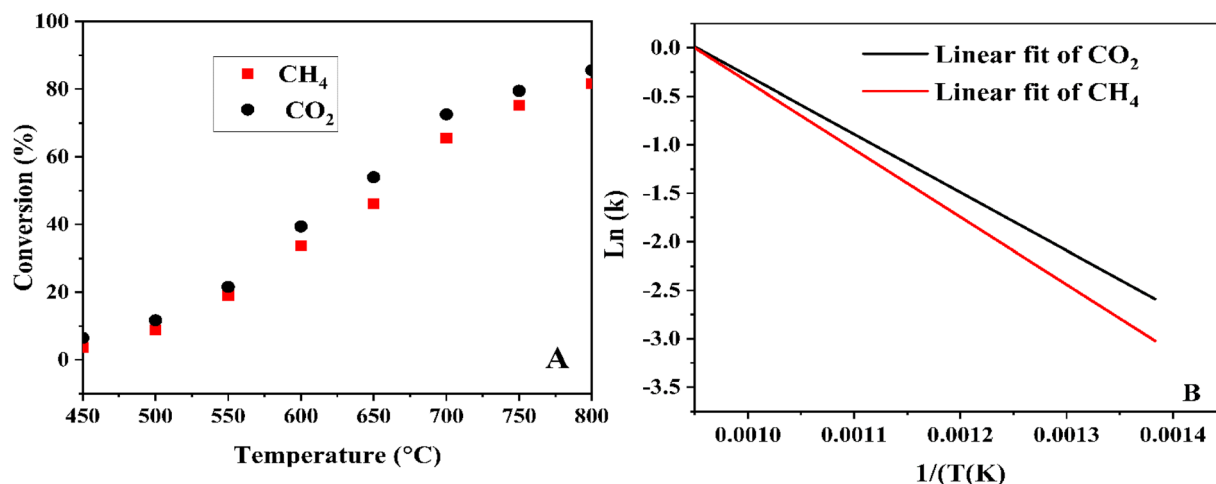

Fig. 4 Reaction temperatures on CH_4 and CO_2 conversions (A) and their corresponding linear fits using the Arrhenius equation (B).

Table 3 The feed (CH_4 and CO_2) conversions for different reaction temperatures

T (°C)	T (K)	% CH_4 conv.	CH_4 conv.	% CO_2 conv.	CO_2 conv.	CH_4 $\ln(k)$	CO_2 $\ln(k)$	$1/T$ (K)
450	723	3.66	0.0366	6.5	0.065	−3.3077	−2.7334	0.00138
500	773	8.74	0.0874	11.7	0.117	−2.4373	−2.1456	0.00129
550	823	18.96	0.1896	21.6	0.216	−1.6628	−1.5325	0.00122
600	873	33.75	0.3375	39.39	0.3939	−1.0862	−0.9317	0.00115
650	923	46.06	0.4606	53.98	0.5398	−0.7752	−0.6166	0.00108
700	973	65.5	0.655	72.6	0.726	−0.4231	−0.3202	0.00103
750	1023	75.2	0.752	79.5	0.795	−0.285	−0.2294	0.00098
800	1073	81.6	0.816	85.6	0.856	−0.2033	−0.1555	0.00093

Table 4 The computed parameters of the Arrhenius equation

	CH_4	CO_2
Intercept	6.62	5.72
Slope	−6969.6	−6004.5
Pre-exponential factor (A)	749.0	303.5
Activation energy (E_a)	56.7 kJ mol^{-1}	48.8 kJ mol^{-1}

Table 5 Actual and coded values for the process parameters

	Levels	
Process parameter	Low	High
Gas hour space velocity (ccg^{-1} h^{-1})[a]	22 000	42 000
Temperature (°C)	700	800
CH_4/CO_2	0.5	1

[a] Gas hour space velocity (ccg^{-1} h^{-1}) = the space velocity is based only on CH_4 and CO_2, excluding N_2.

normalizing or equalizing the variance of the response data.[32] The variance analysis and prediction statistics presented in Table 6 were computed to assess the adequacy of the regression models. Elevated F-values and low-significance P-values suggest the significance of the models, encompassing all terms in the polynomial equations within the approximately 95% confidence limits. The substantial R^2 values indicate the well-fitted nature of all experimental results within the models, as suggested by Fig. 9. A coefficient with P-values below 0.05 implies a significant effect on the response, considering a 95% confidence level. A more decisive criterion involves calculating an F-value defined by eqn (15):

$$F_{calc.} = \frac{\sum_{i=1}^{N}(y_i - y_{ci})^2}{(N - c)} \Bigg/ S^2 \tag{15}$$

where N represents the total number of observations or data points, the variance of replicate readings at the center of the design is denoted as S^2, and c represents the count of eliminated coefficients (those rejected or deemed insignificant for the response) in the regression equation. This is then juxtaposed with the critical F-value derived, for example, from the FINV function in Excel, with degrees of freedom for the

numerator (d.f.n) equal to $(N - c)$ and degrees of freedom for the denominator (d.f.d) equal to $(r - 1)$, where r is the number of replications at the center of the design. At a significance level of 0.05, if the calculated F-value ($F_{calc.}$) is less than the tabulated F-value (F_{table}), it signifies that the obtained regression equation model adequately fits the experimental data. The examination of the regression models' validity involved comparing the predicted responses with their respective experimental data in Table 7. Fig. 5 shows the plots of the actual values of CH_4 and CO_2 conversion and H_2/CO ratio and their comparable predicted values from the CCD model. The proximity of data to the 45° straight line affirms the model's reliability, where there are robust correlations between the actual (experimental) data and their predicted values derived from the CCD model.[33–35]

Here df (degrees of freedom) represents the number of values in the final calculation of a statistic that are free to vary, the F-value is the ratio of error mean square to model mean square, and the P-value is the probability of observing a value of F greater than what was observed, assuming equal means in various populations. For more details, see, for example, in ref. 33–35.

3.9.2 Final equation in terms of actual factors. Based on the experimental data, employing ANOVA at a significance level (α) of 0.05 and subsequent identification of significant factor effects while excluding the insignificant ones, and utilizing Design-Expert software version 13, the best models have been suggested as follows.

$$
\begin{aligned}
CH_4 \text{ conversion } \% = {}& -653.27355 + 1.99989 \times T - 0.003098 \\
& \times SV - 91.447 \times CH_4/CO_2 + 0.0000035 \times T \times SV \\
& + 0.0985 \times T \times CH_4/CO_2 - 0.0003 \times SV \times CH_4/CO_2 \\
& - 0.001312 \times T^2
\end{aligned} \tag{16}
$$

$$
\begin{aligned}
CO_2 \text{ conversion } \% = {}& -119.3866 + 0.19606 \times T - 0.000509 \\
& \times SV + 89.408 \times CH_4/CO_2 - 27.824 \times (CH_4/CO_2)^2
\end{aligned} \tag{17}
$$

$$
\begin{aligned}
H_2/CO = {}& 1.00133 - 0.00097 \times T + 0.0000011 \times SV \\
& - 0.1219 \times CH_4/CO_2 + 0.00173 \times T \times CH_4/CO_2 - 0.0000031 \\
& \times SV \times CH_4/CO_2 - 0.4648 \times (CH_4/CO_2)^2
\end{aligned} \tag{18}
$$

The models incorporate intercept term coefficients signifying the expected response variable value when all factors are zero. Additionally, they encompass main effects, denoting the linear impact of factors, representing the change in the response variable for a one-unit increase in the factor while

Table 6 Statistics and analysis of variance for multiple regression and various components

Source	Sum of squares	df	Mean square	F-value	P-value
Response 1: CH$_4$ conversion reduced quadratic model (R^2 = 0.9668)					
Model	2203.19	7	314.74	41.59	<0.0001
A = temperature	1205.16	1	1205.16	159.24	<0.0001
B = space velocity[a]	447.69	1	447.69	59.15	<0.0001
C = CH$_4$/CO$_2$ ratio	460.91	1	460.91	60.9	<0.0001
AB	25.03	1	25.03	3.31	0.099
AC	12.13	1	12.13	1.6	0.2342
BC	4.49	1	4.49	0.5926	0.4592
A^2	47.79	1	47.79	6.31	0.0308
Response 2: CO$_2$ conversion reduced quadratic model (R^2 = 0.9968)					
Model	2653.59	4	663.4	1025.17	<0.0001
A = temperature	960.99	1	960.99	1485.05	<0.0001
B = space velocity[a]	258.78	1	258.78	399.89	<0.0001
C = CH$_4$/CO$_2$ ratio	1420.39	1	1420.39	2194.97	<0.0001
C^2	13.44	1	13.44	20.77	0.0005
Response 3: H$_2$/CO – reduced quadratic model (R^2 = 0.9956)					
Model	0.1001	6	0.0167	163.61	<0.0001
A = temperature	0.0027	1	0.0027	26.37	0.0003
B = space velocity[a]	0.0018	1	0.0018	17.87	0.0014
C = CH$_4$/CO$_2$ ratio	0.0876	1	0.0876	858.8	<0.0001
AC	0.0037	1	0.0037	36.67	<0.0001
BC	0.0005	1	0.0005	5.18	0.0439
C^2	0.0038	1	0.0038	36.77	<0.0001

[a] Space velocity = the space velocity is based only on CH$_4$ and CO$_2$, excluding N$_2$.

Table 7 Experimental (exp.) data and predicted (pred.) results for various components of the reaction system

	Factors			CH$_4$ conversion %			CO$_2$ conversion %			H$_2$/CO		
Run	T	SV[a]	CH$_4$/CO$_2$	Exp.	Pred.	MAPE	Exp.	Pred.	MAPE	Exp.	Pred.	MAPE
1	700	32 000	0.75	59.67	60.02	0.59	51.35	52.98	3.17	0.825	0.8349	1.20
2	750	32 000	0.75	73.9	74.28	0.51	62.5	62.79	0.46	0.848	0.8513	0.39
3	800	32 000	0.75	84.78	81.97	3.31	73.36	72.59	1.05	0.882	0.8677	1.62
4	700	22 000	0.5	76.84	75.75	1.42	44.89	44.41	1.07	0.746	0.7392	0.91
5	750	22 000	0.75	83.87	80.97	3.46	68.69	67.87	1.19	0.875	0.8648	1.17
6	700	42 000	1	46.18	42.79	7.34	58.03	58.07	0.07	0.865	0.8562	1.02
7	750	42 000	0.75	65.89	67.58	2.56	58.36	57.7	1.13	0.831	0.8378	0.82
8	750	32 000	0.5	83.69	81.06	3.14	49.45	49.13	0.65	0.738	0.7286	1.27
9	750	32 000	1	65.51	67.49	3.02	72.89	72.96	0.10	0.905	0.9158	1.19
10	800	22 000	1	83.54	82.09	1.74	88.64	87.85	0.89	0.974	0.9755	0.15
11	750	32 000	0.75	73.9	74.28	0.51	62.5	62.79	0.46	0.848	0.8513	0.39
12	750	32 000	0.75	74.1	74.28	0.24	62.84	62.79	0.08	0.849	0.8513	0.27
13	700	42 000	0.5	58.26	60.33	3.55	35.23	34.24	2.81	0.723	0.7285	0.76
14	800	42 000	0.5	84.81	83.36	1.71	53.17	53.84	1.26	0.723	0.718	0.69
15	750	32 000	0.75	73.34	74.28	1.28	62.68	62.79	0.18	0.852	0.8513	0.08
16	800	42 000	1	69.04	70.75	2.48	77.36	77.68	0.41	0.933	0.9322	0.09
17	800	22 000	0.5	87.7	91.71	4.57	62.9	64.02	1.78	0.713	0.7288	2.22
18	700	22 000	1	59.14	61.21	3.50	67.9	68.25	0.52	0.902	0.8994	0.29
					Mean	2.50		Mean	0.96		Mean	0.81

[a] SV = the space velocity is based only on CH$_4$ and CO$_2$, excluding N$_2$.

keeping other factors constant. The models also include terms accounting for quadratic effects, capturing nonlinear relationships between the factors and the response variable.

According to the coefficient of the determination R^2, eqn (19), which is a statistical metric on a convenient scale ranging from 0% to 100%, indicating the adequacy of fit in the models, essentially gauging how well the model aligns with the data. The first fitted model explains that around 96.68% of the CH$_4$ conversion variation, the second explains around 99.68% of the CO$_2$ conversion variation, and the third model explains around
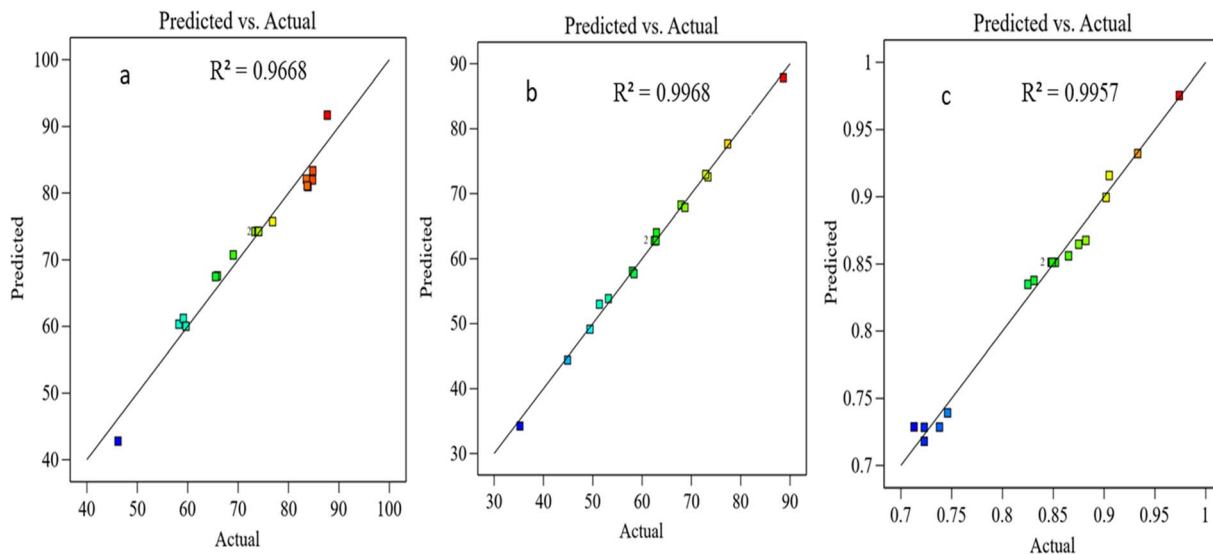
Fig. 5 The experimental and predicted data for (a) CH_4 conversion, (b) CO_2 conversion, and (c) H_2/CO ratio.

99.56% of the H_2/CO variation: the remaining variations are attributed to factors beyond the scope of the experiment. It is noteworthy that the overall variation in the response variable (SS_{total}) is divided into two components. The sum of squares attributed to the fitted model (SS_{model}) and the unexplained variation, represented by the sum of squares due to errors (SS_{error}) in eqn (20). A higher R^2 value indicates a more precise description of the relationship between variables, as it corresponds to a smaller SS_{error}.

$$R^2 = \frac{SS_{model}}{SS_{total}} = 1 - \frac{SS_{error}}{SS_{total}} \tag{19}$$

$$\underbrace{\sum_{i=1}^{n} \left(E_i - \overline{E}\right)^2}_{SS_{total}} = \underbrace{\sum_{i=1}^{n} \left(P_i - \overline{E}\right)^2}_{SS_{model}} + \underbrace{\sum_{i=1}^{n} \left(E_i - P_i\right)^2}_{SS_{error}} \tag{20}$$

where n is the total number of experiments, E_i and P_i denote the experimental/actual and predicted values of the ith observation, and $\overline{E}$ is the mean value of the response variable across all observations.

In the following, Table 6 represents the experimental and predicted values of the response variables according to the suggested models (16)–(18).

As demonstrated in Table 7, the proximity observed between the predicted responses from the fitted models and the actual values is evident in the low absolute error rates for each case, as indicated by the mean absolute error percentage. We have MAPEs = 2.50, 0.96, and 0.81 for the fitted models of CH_4 and CO_2 conversions and H_2/CO, respectively. The MAPE formula is shown in eqn (16).

3.9.3 Models' accuracy. The precision of the predicted models determined through the application of the Central Composite Design (CCD) methodology, underwent evaluation using various mathematical metrics. These included R^2, as presented in eqn (12), absolute percentage error (APE), mean absolute percentage error (MAPE) and mean absolute errors

(MAE) detailed in eqn (21) through (23). A graphical representation of predicted *versus* actual values serves as a means to assess the model's performance and compare it to the null model. In the case of a well-fitted model, the points should closely align with the fitted line, characterized by narrow confidence bands. Points deviating significantly from the mean exert more influence on the fitted line, while those considerably distant from the line might signify potential outliers. Both of these factors can negatively affect the fit of the model. Fig. 5a–c represent the actual and predicted values of the response variables, CH_4 conversion and CO_2 conversion and H_2/CO respectively. It is observed that the predicted and actual values are close to the straight line X(actual) = Y(predicted); this is another indication of the quality and accuracy of the suggested models. Also, as shown in the regression analysis results in Table 5, there is a strong correlation (R^2 near to 1) between the predicted CCD models and experimental values. Overall, it is observed that there is a good agreement between the model's predictions and the experimental data.

$$APE = 100 \times \frac{|E_i - P_i|}{E_i}\% \tag{21}$$

$$MAE = \frac{1}{n} \sum_{i=1}^{n} \frac{|E_i - P_i|}{E_i} \tag{22}$$

$$MAPE = 100 \times \frac{1}{n} \sum_{i=1}^{n} \frac{|E_i - P_i|}{E_i}\% \tag{23}$$

3.9.4 Simulation of the Design Expert program

3.9.4.1 One factor effect (2D) plot. The effect of each process parameter on the reaction responses at A (temperature) = 750 °C, B (SV) = 32 000 ccg^{-1} h^{-1} and C ($CH_4 : CO_2$) = 0.75 is shown in Fig. 6. Fig. 6A indicates that increasing the temperature, decreasing the GHSV value, and decreasing the $CH_4 : CO_2$ ratio will increase CH_4 conversion. Fig. 6B indicates that increasing
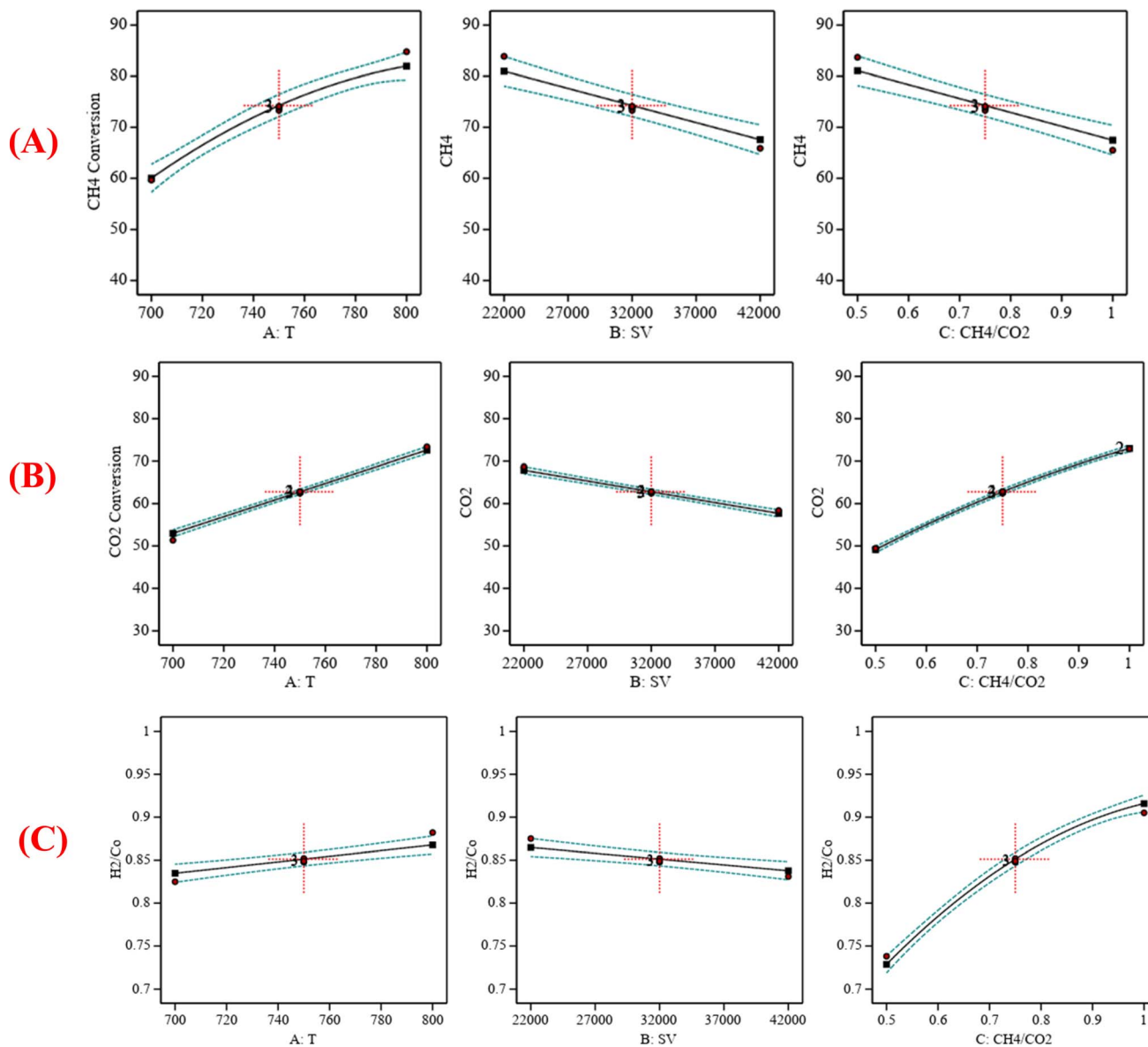
Fig. 6 (A) The relationship between the reaction parameters and CH_4 conversion percentage; (B) the relationship between the reaction parameters and CO_2 conversion percentage; (C) the relationship between the reaction parameters and H_2/CO ratio.

the temperature, decreasing the GHSV value, and increasing the $CH_4 : CO_2$ ratio will increase CO_2 conversion. Fig. 6C indicates that increasing the temperature, decreasing the GHSV value, and increasing the $CH_4 : CO_2$ ratio will increase H_2/Co.

3.9.4.2 Two factor effect (3D plot). Employing the values of the regression parameters for various components portrayed resulting from eqn (9)–(11) resulted in the following graphical models of RSM, which represent the conversion or formation of the various components of the reaction system in terms of the coded independent variables. The equations expressed in actual factor terms enable predictions about the responses for specified levels of each factor. It is crucial to specify these levels in the original units corresponding to each factor. Using these equations, the Design Expert program facilitated the construction of response surface plots depicting the anticipated conversion or formation of different components in the reaction system. This

visualization considered two process variables, while the third was held at a constant level or value, as illustrated in Fig. 7–9. Fig. 7 shows the three-dimensional response surface plot, which represents the significant effects of the factors (temperature, GHSV, and $CH_4 : CO_2$) on the variation of the response variable CH_4 conversion. Fig. 7A shows the surface plots, which represent the functional relationship between a designated response variable (CH_4 conversion) and the two-factor variables (temperature and gas hourly space velocity) with a $CH_4 : CO_2$ feed ratio fixed at 0.75. It represents how these factors have significant effects on the variation of CH_4 conversion. The response surface shows that with increasing the temperature and decreasing the GHSV, the CH_4 conversion increases. It was observed to increase from 46.18% at 700 °C to 87.7% at 800 °C. Fig. 7B shows the surface plots that represent the functional relationship between a designated response variable (CH_4
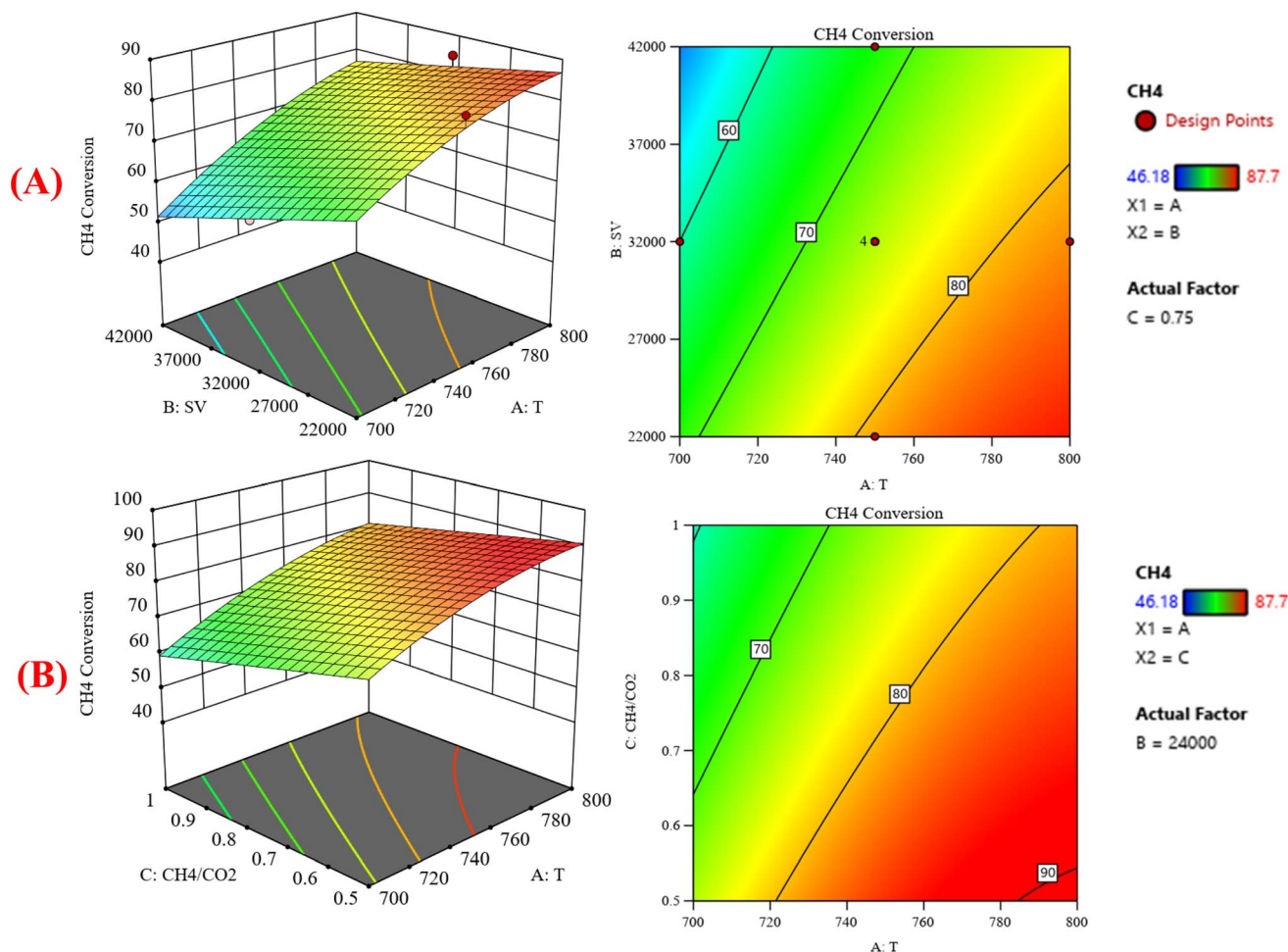
Fig. 7 The relationship between the temperature (A) GHSV and CH_4 conversion % with $CH_4 : CO_2$ fixed at 0.75, (B) $CH_4 : CO_2$, and CH_4 conversion % with GHSV (the space velocity) fixed at 24 000.

conversion) and the two factor variables (temperature and CH_4 : CO_2) with GHSV fixed at 24 000 ccg^{-1} h^{-1}. The response surface shows that with increasing the temperature and decreasing the $CH_4 : CO_2$, the CH_4 conversion increases. Because dry reforming of methane is an endothermic reaction, the conversion of CH_4 is expected to be temperature-sensitive. These discoveries may be useful in optimizing the conditions for methane dry reforming and increasing the process's efficiency. Fig. 8 shows the three-dimensional response surface plot that represents the significant effects of the factors (temperature, GHSV and $CH_4 : CO_2$) on the variation of the response variable CO_2 conversion. In Fig. 8A, the response surface plot shows at $CH_4 : CO_2 = 0.78$ and with increasing the temperature and decreasing the GHSV, the CO_2 conversion increases from 35.23% at 700 °C to 88.64% at 800 °C. Generally, the operating temperature displayed almost a linear relationship with the conversion. This is ascribed to the endothermic nature of the DRM.[36,37] Reports have shown that the dry reforming reaction is thermodynamically favored at the temperature range of 650–800 °C [38–40]. Both CH_4 and CO_2 conversions steadily decrease with increasing GHSV. This shows that GHSV influences activity, where a steady drop in CH_4 conversion was observed with increasing GHSV. This is in

accord with literature findings, which indicated that the higher the GHSV, the smaller the contact time for CH_4 molecules to interact with active sites.[38,39]

Fig. 8B represents that at constant GHSV at 23 800, the CO_2 conversion increased from 35.2% to 88.6% as temperature increased from 700 °C to 800 °C. Fig. 9A shows the surface plots that represent the suggested model that represents the relationship between the response variable syngas production (H_2/CO) and the factor variables (temperature and gas hourly space velocity) with fixed $CH_4 : CO_2$ at 0.91. It represents the significant effects of these factors on the variation of H_2/CO. The three-dimensional response surface shows that with increasing the temperature and decreasing the gas hour space velocity, the H_2/CO increases to reach its maximum value. H_2/CO increase from 0.713–0.974 at 700–800 °C. The same range of variation of H_2/CO is observed in Fig. 9B, which shows the relationship between the response variable H_2/CO and the factor variables (temperature and $CH_4 : CO_2$) with fixed gas hourly space velocity SV at 27 000. This corresponds to an increase in CH_4 conversion under these conditions because the creation of hydrogen-rich syngas might be attributed to methane dissociation: $CH_4 \rightarrow C + H_2$ on the surface of the catalyst, leading to an increase in the
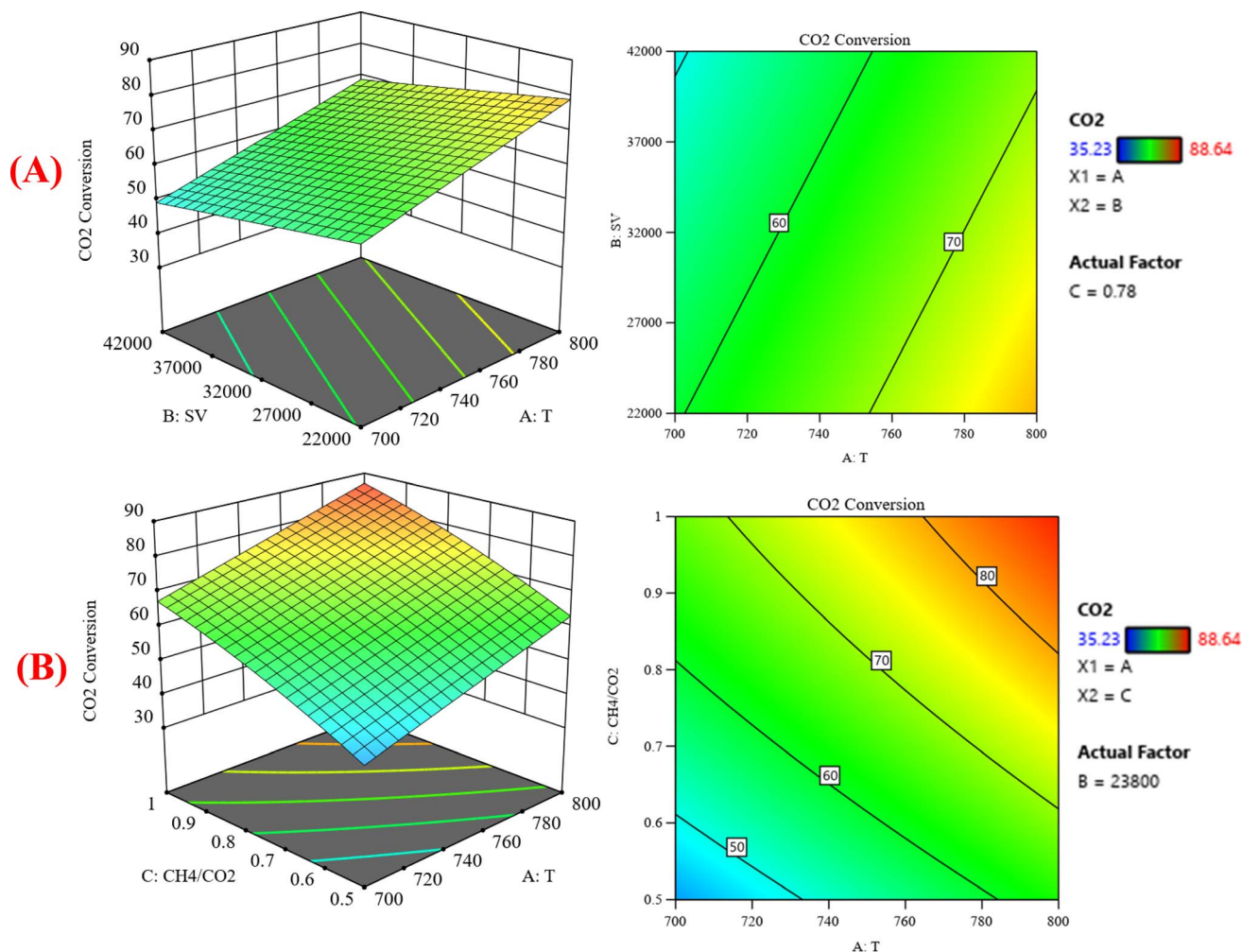
Fig. 8 The relationship between the temperature (A) GHSV, and CO_2 conversion % with $CH_4 : CO_2$ fixed at 0.78; (B) $CH_4 : CO_2$, and CO_2 conversion % with GHSV (the space velocity) fixed at 23 800.

selectivity of H_2. This discovery is consistent with the literature, which has documented methane dissociations as rate-determining steps in dry reforming reactions.[36] Similarly, an increase in temperature significantly increases H_2 selectivity.

3.9.5 Process optimization. The process optimization involved maximizing the response variables (CH_4 conversion, CO_2 conversion, and the H_2/Co ratio) using Design-Expert version 13, which incorporates optimization goals to yield multiple solutions meeting the specified criteria. The optimal conditions were selected based on the solution with the highest desirability value.[37] Each set of the process conditions, that is, temperature, GHSV, and $CH_4 : CO_2$, was subjected to the models present in eqn (9)–(11) to obtain predicted goals in Table 8. Optimization aims to pinpoint a satisfactory set of conditions that will fulfill all objectives. After getting the combined optimum condition values of temperature (800 °C), GHSV (22 000), and $CH_4 : CO_2$ (1.00) from the optimization procedure, the same circumstances were tested experimentally in the reactor, and the results, as given in Table 7, closely resembled (5% difference) the predicted values.

3.10 Economic aspects of the proposed catalytic process

To determine whether the proposed catalytic process for syngas production is feasible, we need to evaluate its economic aspects. Specifically, we must consider the cost of producing the NiRh/SiAl catalyst, which is dependent on the cost of Ni, Rh, and silica–alumina. Since Rh is an expensive metal, it could have a significant impact on the overall cost of the catalyst. The cost of producing the NiRh/SiAl catalyst depends on the complexity of the synthesis method used. As compared to conventional catalysts used for syngas production, such as steam reforming catalysts based on Ni, the presence of Rh in NiRh/SiAl may increase the production cost. The operational costs of the catalytic process would include the cost of CH_4 as the primary reactant, the energy required to maintain the reaction temperature, and the frequency of catalyst replacement due to deactivation will impact operational costs. The long-term stability and reusability of NiRh/SiAl compared to other catalysts become crucial factors. Techniques for regenerating catalysts, such as steam or oxygen pulses, can impact operational costs. When compared to traditional methods like steam reforming, which is
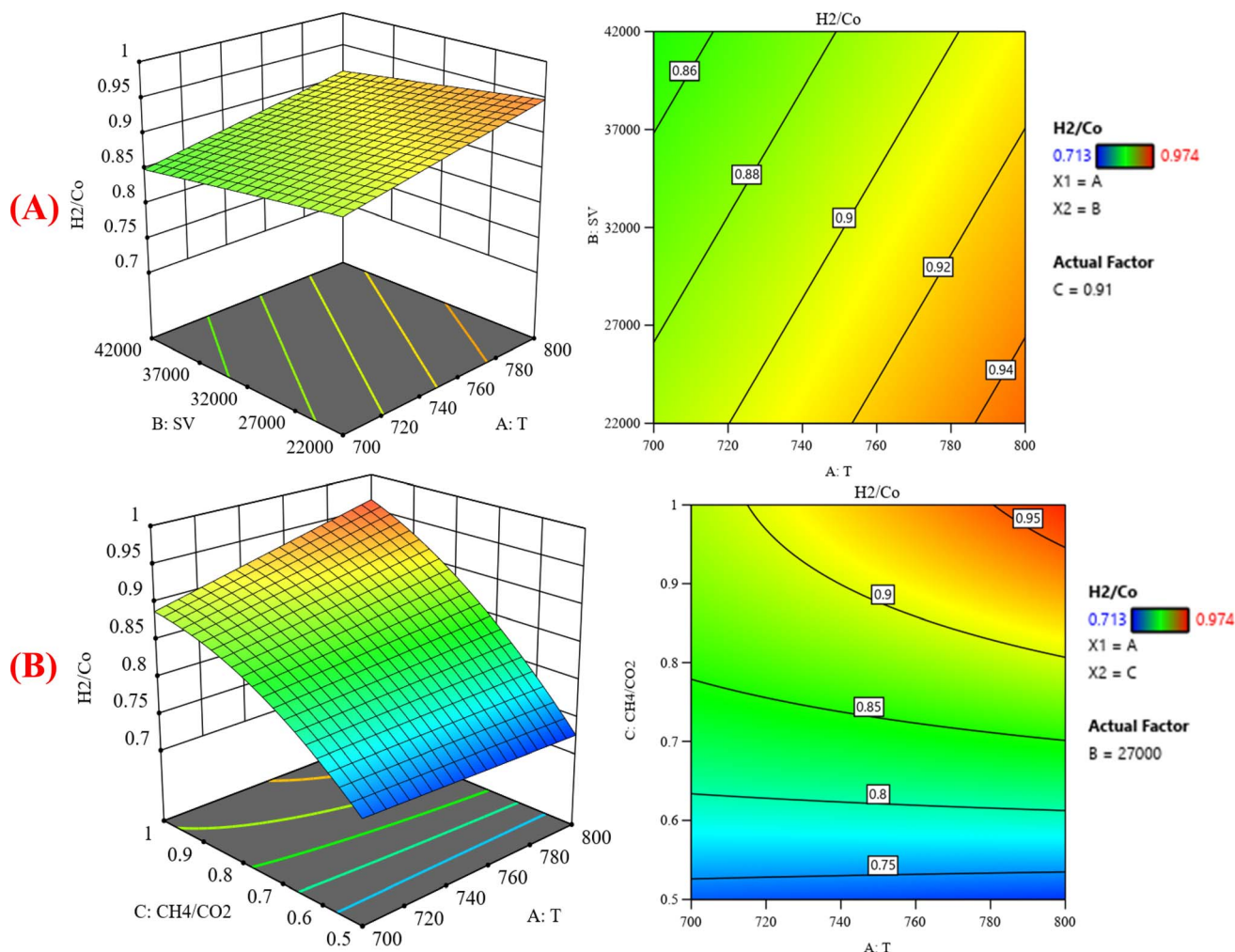
Fig. 9 The relationship between the temperature (A) GHSV and H_2/CO % with $CH_4 : CO_2$ fixed at 0.91; (B) H_2/CO and GHSV% with GHSV (the space velocity) fixed at 27 000.

Table 8 The optimal goals and optimum conditions

Goals function		Variables					
		Temp.	SV[a]	CH_4/CO_2	CH_4 con.	CO_2 con.	H_2/CO
Max (CH_4 conversion)	Criteria	In range	In range	In range	Max.	In range	In range
	Optimum conditions.	787.3	22 459.4	0.613	88.586	67.916	0.803
Max (CO_2 conversion)	Criteria	In range	In range	In range	In range	Max.	In range
	Optimum conditions.	800.0	22 000.3	0.995	82.193	87.667	0.974
Max (H_2/CO)	Criteria	In range	In range	In range	In range	In range	Max.
	Optimum conditions.	799.9	22 089.8	0.999	82.043	87.757	0.975
Max (CH_4-conversion) & max	Criteria	In range	In range	In range	Max.	Max.	Max.
(CO_2-conversion) & max (H_2/CO)	Optimum conditions.	800.0	22 000.0	1.000	82.087	87.854	0.975
Experimental	Optimum conditions	800.0	22 000.0	1.000	86.99	93.11	0.99

[a] SV = the space velocity is based only on CH_4 and CO_2, excluding N_2.

widely used for producing syngas from natural gas, the initial implementation cost may be lower due to less expensive catalysts. However, steam reforming has limitations as it requires high temperatures, leading to increased energy consumption. It is also less selective in product formation, which necessitates

additional processing steps. The autothermal reforming (ATR) method, on the other hand, combines steam reforming with partial oxidation and thus has the potential to decrease energy costs. However, ATR catalysts may be vulnerable to deactivation and, as a result, require frequent replacement. Although the

NiRh/SiAl catalyst has shown promise in efficiently producing syngas, a more detailed techno-economic analysis is required. This analysis should involve estimating the costs involved in catalyst production and operation, as well as comparing it with existing production methods. Additionally, it should consider market prices of syngas and potential credits for cleaner production processes. By assessing all economic aspects, one can determine if the proposed catalytic process offers a cost-effective and viable solution for syngas production.

4. Conclusions

A study explored using nickel (Ni) catalysts with different promoters (Ir, Pt, Pd, Ru, and Rh) on silica–alumina (SiAl) for dry reforming of methane (DRM), a method to convert methane into syngas (H_2 and CO). The most effective catalyst was NiRh/SiAl, achieving the highest methane (65.2%) and carbon dioxide (CO_2) (71.5%) conversion rates among those tested due to high surface area, homogeneity in pore size distribution, maximum degree of reduction, and higher side of NiO's reducibility which undergoes moderate interaction with the support. It also showed good stability, with only a 5% weight loss after the experiment. Other catalysts (NiIr/SiAl, NiPd/SiAl, NiPt/SiAl, and NiRu/SiAl) had lower conversion rates, ranging from 38.8% to 46.3% for methane and 43.7% to 57.5% for CO_2. The inferior catalytic activity of the Ir-promoted catalyst is due to the deposition of graphitic-type carbon more pronouncedly over the active sites. NiRh/SiAl outperforms other catalysts and this catalyst is further selected for process optimization under central composite design. Catalytic activity, like CH_4 conversion and CO_2 conversion, is presented as a response which is correlated to experimental factors like temperature, feed ratio and catalyst concentration by the predictive model. Researchers found that a specific catalyst (Rh-promoted Ni/SiAl) achieved high conversion rates for methane and carbon dioxide into valuable products while also achieving a desirable ratio of hydrogen to carbon monoxide. This success highlights the effectiveness of a statistical method (central composite design) for optimizing these methane-reforming processes. This study suggests that these catalysts have promise for industrial applications due to their efficiency and ability to reduce greenhouse gas emissions. The central composite design statistical method was used to predict ideal conditions for a process that converts CH_4 and CO_2 into useful products. Experiments confirmed that this method was accurate. At a temperature of 800 °C and a flow rate of 22 000 ml $(h^{-1} g_{cat}^{-1})$, a catalyst made of Ni and Rh on a SiAl base achieved excellent results: 93.1% of CO_2 conversion, 87.0% of CH_4 conversion, and a H_2 to CO ratio of 0.99. This study shows that this method is a good way to improve the process and that NiRh/SiAl catalysts are promising for reducing greenhouse gas emissions.

Data availability

The datasets generated and/or analyzed during the current study are available from the corresponding author on reasonable request. Specific data include: (1) Raw data: the raw experimental data from the sustainable energy and fuel study, including initial measurements and observations, are stored in a secure institutional repository and can be accessed upon request to the corresponding author. (2) Processed data: processed data that support the findings of this study are available in the ESI† of this article. This includes detailed calculations, derived data points, and processed datasets. (3) Supporting Information: additional supporting information and detailed methodologies are included within the ESI† files attached to this article. Requests for data and materials should be addressed to Ahmed S. Al-Fatesh at aalfaesh@ksu.edu.sa.

Conflicts of interest

There are no conflicts to declare.

References

1 S. C. Doney, V. J. Fabry, R. A. Feely and J. A. Kleypas, Ocean Acidification: The Other CO2 Problem, *Ann. Rev. Mar. Sci*, 2009, **1**, 169–192, DOI: **10.1146/annurev.marine.010908.163834**.

2 J. Hu, P. Hongmanorom, J. Chen, W. Wei, P. Chirawatkul, V. V. Galvita and S. Kawi, Tandem Distributing Ni into CaO Framework for Isothermal Integration of CO2 Capture and Conversion, *Chem. Eng. J.*, 2023, **452**(P3), 139460, DOI: **10.1016/j.cej.2022.139460**.

3 N. Abas, A. Kalair and N. Khan, Review of Fossil Fuels and Future Energy Technologies, *Futures*, 2015, **69**, 31–49, DOI: **10.1016/j.futures.2015.03.003**.

4 P. Tomkins and T. E. Müller, Evaluating the Carbon Inventory, Carbon Fluxes and Carbon Cycles for a Long-Term Sustainable World, *Green Chem.*, 2019, **21**(15), 3994–4013, DOI: **10.1039/c9gc00528e**.

5 C. Zhang, Y. Li, Z. Chu, Y. Fang, K. Han and Z. He, Analysis of Integrated CO2 Capture and Utilization *via* Calcium-Looping in-Situ Dry Reforming of Methane and Fischer-Tropsch for Synthetic Fuels Production, *Sep. Purif. Technol.*, 2024, **329**, 125109, DOI: **10.1016/j.seppur.2023.125109**.

6 Y. Sha, Y. Ling, Y. Yang, X. Wang, D. Meng and S. Wang, A Finger-like Anode with Infiltrated Ni0.1Ce0.9O2-δ Catalyst Using New Phase Inversion Combined Tape-Casting Technology for Optimized Dry Reforming of Methane, *Ceram. Int.*, 2023, **49**(17), 29155–29163, DOI: **10.1016/j.ceramint.2023.06.195**.

7 Y. Lei, J. Ye, J. García-Antón and H. Liu, Recent Advances in the Built-in Electric-Field-Assisted Photocatalytic Dry Reforming of Methane, *Chin. J. Catal.*, 2023, **53**, 72–101, DOI: **10.1016/S1872-2067(23)64520-6**.

8 S. A. Al-Zahrani, A. S. Al-Fatesh, M. N. Kaydouh, A. Al Otaibi, F. Francesco, A. H. Fakeeha and N. El Hassan, High Carbon-

Resistant Nickel Supported on Yttria–Zirconia Catalysts for Syngas Production by Dry Reforming of Methane: The Promoting Effect of Cesium, *Alexandria Eng. J.*, 2023, **74**, 371–386, DOI: **10.1016/j.aej.2023.05.040**.

9 X. Yuan, B. Li, X. Wang and B. Li, Synthesis Gas Production by Dry Reforming of Methane over Neodymium-Modified Hydrotalcite-Derived Nickel Catalysts, *Fuel Process. Technol.*, 2022, **227**, 107104, DOI: **10.1016/j.fuproc.2021.107104**.

10 D. Liang, Y. Wang, Y. Wang, M. Chen, X. Xie, C. Li, J. Wang and L. Yuan, Dry Reforming of Methane for Syngas Production over Noble Metals Modified M-Ni@S-1 Catalysts (M = Pt, Pd, Ru, Au), *Int. J. Hydrogen Energy*, 2023, 1–14, DOI: **10.1016/j.ijhydene.2023.07.135**.

11 H. Er-rbib, C. Bouallou and F. Werkoff, Dry Reforming of Methane - Review of Feasibility Studies, *Chem. Eng. Trans.*, 2012, **29**, 163–168, DOI: **10.3303/CET1229028**.

12 L. Zhu, L. Li and J. Fan, A Modified Process for Overcoming the Drawbacks of Conventional Steam Methane Reforming for Hydrogen Production: Thermodynamic Investigation, *Chem. Eng. Res. Des.*, 2015, **104**, 792–806, DOI: **10.1016/j.cherd.2015.10.022**.

13 R. Kumar, A. Kumar and A. Pal, Overview of Hydrogen Production from Biogas Reforming: Technological Advancement, *Int. J. Hydrogen Energy*, 2022, **47**(82), 34831–34855, DOI: **10.1016/j.ijhydene.2022.08.059**.

14 A. I. Osman, A. Ayati, P. Krivoshapkin, B. Tanhaei, M. Farghali, P.-S. Yap and A. Abdelhaleem, Coordination-driven innovations in low-energy catalytic processes: advancing sustainability in chemical production, *Coord. Chem. Rev.*, 2024, **514**, 215900, DOI: **10.1016/j.ccr.2024.215900**.

15 Y. Wang, L. Yao, S. Wang, D. Mao and C. Hu, Low-Temperature Catalytic CO2 Dry Reforming of Methane on Ni-Based Catalysts: A Review, *Fuel Process. Technol.*, 2018, 199–206, DOI: **10.1016/j.fuproc.2017.10.007**.

16 S. Arora and R. Prasad, An Overview on Dry Reforming of Methane: Strategies to Reduce Carbonaceous Deactivation of Catalysts, *RSC Adv.*, 2016, **6**(110), 108668–108688, DOI: **10.1039/c6ra20450c**.

17 A. I. Tsyganok, M. Inaba, T. Tsunoda, K. Suzuki, K. Takehira and T. Hayakawa, Combined Partial Oxidation and Dry Reforming of Methane to Synthesis Gas over Noble Metals Supported on Mg–Al Mixed Oxide, *Appl. Catal., A*, 2004, **275**(1–2), 149–155, DOI: **10.1016/J.APCATA.2004.07.030**.

18 A. Choya, B. de Rivas, M. L. No, J. I. Gutiérrez-Ortiz and R. López-Fonseca, Dry Reforming of Methane over Sub-Stoichiometric NiAl2O4-Mediated Ni/Al2O3 Catalysts, *Fuel*, 2024, **358**, 130166, DOI: **10.1016/j.fuel.2023.130166**.

19 P. K. Yadav and S. Sharma, Ni, Co & Cu Substituted CeO2: A Catalyst That Improves H2/CO Ratio in the Dry Reforming of Methane, *Fuel*, 2024, **358**(PB), 130163, DOI: **10.1016/j.fuel.2023.130163**.

20 A. Trovarelli and J. Llorca, Ceria Catalysts at Nanoscale: How Do Crystal Shapes Shape Catalysis?, *ACS Catal.*, 2017, **7**(7), 4716–4735, DOI: **10.1021/acscatal.7b01246**.

21 X. Hong, B. Li, Y. Wang, J. Lu, G. Hu and M. Luo, Stable Ir/SiO 2 Catalyst for Selective Hydrogenation of Crotonaldehyde, *Appl. Surf. Sci.*, 2013, **270**, 388–394, DOI: **10.1016/j.apsusc.2013.01.035**.

22 A. K. Mageed, B. V. Ayodele and S. I. Mustapa, Response Surface Optimization of Hydrogen-Rich Syngas Production by Greenhouse Gases Reforming, *Chem. Eng. Technol.*, 2020, **43**(4), 742–751, DOI: **10.1002/ceat.201900475**.

23 Z. Bian, W. Zhong, Y. Yu, Z. Wang, B. Jiang and S. Kawis, Dry Reforming of Methane on Ni/Mesoporous-Al2O3 Catalysts, Effect of Calcination Temperature, *Int. J. Hydrogen Energy*, 2021, **46**, 31041–31053, DOI: **10.1016/j.ijhydene.2020.12.064**.

24 R. Fiorenza, L. Spitaleri, A. Gulino and S. Scirè, Ru–Pd Bimetallic Catalysts Supported on CeO2-MnOx Oxides as Efficient Systems for H2 Purification through CO Preferential Oxidation, *Catalysts*, 2018, **8**(5), 1–18, DOI: **10.3390/catal8050203**.

25 J. N. Park, J. Kuk Shon, M. Jin, S. Sung Kong, K. Moon, G. Ok Park, J. H. Boo and J. Man Kim, Room-Temperature CO Oxidation over a Highly Ordered Mesoporous RuO 2 Catalyst, *React. Kinet., Mech. Catal.*, 2011, **103**(1), 87–99, DOI: **10.1007/s11144-011-0284-5**.

26 A. Osaka, T. Takatsuna and Y. Miura, Iridium Oxide Films *via* Sol-Gel Processing, *J. Non-Cryst. Solids*, 1994, **178**(C), 313–319, DOI: **10.1016/0022-3093(94)90300-X**.

27 M. Zimowska, J. B. Wagner, J. Dziedzic, J. Camra, B. Borzęcka-Prokop and M. Najbar, Some Aspects of Metal-Support Strong Interactions in Rh/Al 2O3 Catalyst under Oxidising and Reducing Conditions, *Chem. Phys. Lett.*, 2006, **417**(1–3), 137–142, DOI: **10.1016/j.cplett.2005.09.112**.

28 A. Jorio and R. Saito, Raman Spectroscopy for Carbon Nanotube Applications, *J. Appl. Phys.*, 2021, **129**, 021102, DOI: **10.1063/5.0030809**.

29 R. Baddour-Hadjean and J. P. Pereira-Ramos, Raman Microspectrometry Applied to the Study of Electrode Materials for Lithium Batteries, *AIP Conf. Proc.*, 2010, **1267**, 1137–1138, DOI: **10.1063/1.3482342**.

30 R. Saito, A. Grüneis, G. G. Samsonidze, V. W. Brar, G. Dresselhaus, M. S. Dresselhaus, A. Jorio, L. G. Cançado, C. Fantini, M. A. Pimenta and A. G. Souza Filho, Double Resonance Raman Spectroscopy of Single-Wall Carbon Nanotubes, *New J. Phys.*, 2003, **5**, 157–157, DOI: **10.1088/1367-2630/5/1/157**.

31 W. V. Harper and T. R. James, Concerns about Least Squares Estimation for the Three-Parameter Weibull Distribution: Case Study of Statistical Software, *Jt. Stat. Meet. - Sect. Phys. Eng. Sci.*, 2015, 1268–1282.

32 L. Yang, P. Yin, H. Fan, Q. Xue, K. Li, X. Li, L. Sun and Y. Liu, Response Surface Methodology Optimization of Ultrasonic-Assisted Extraction of Acer Truncatum Leaves for Maximal Phenolic Yield and Antioxidant Activity, *Molecules*, 2017, **22**(2), 232, DOI: **10.3390/molecules22020232**.

33 M. A. Hossain, B. V. Ayodele, C. K. Cheng and M. R. Khan, Optimization of Renewable Hydrogen-Rich Syngas Production from Catalytic Reforming of Greenhouse Gases (CH4 and CO2) over Calcium Iron Oxide Supported Nickel

Catalyst, *J. Energy Inst.*, 2019, **92**(1), 177–194, DOI: **10.1016/j.joei.2017.10.010**.

34 T. Brown, *Section 1. Inq. into Relat. Cause Eff.*, 2013, pp. 323–338, DOI: **10.1017/cbo9781139149747.017**.

35 M. H. Ahmadi Azqhandi, M. Ghaedi, F. Yousefi and M. Jamshidi, Application of Random Forest, Radial Basis Function Neural Networks and Central Composite Design for Modeling and/or Optimization of the Ultrasonic Assisted Adsorption of Brilliant Green on ZnS-NP-AC, *J. Colloid Interface Sci.*, 2017, **505**, 278–292, DOI: **10.1016/j.jcis.2017.05.098**.

36 H. U. Hambali, A. A. Jalil, A. A. Abdulrasheed, T. J. Siang and D. V. N. Vo, Enhanced Dry Reforming of Methane over Mesostructured Fibrous Ni/MFI Zeolite: Influence of Preparation Methods, *J. Energy Inst.*, 2020, **93**(4), 1535–1543, DOI: **10.1016/j.joei.2020.01.016**.

37 A. Abdulrasheed, A. A. Jalil, Y. Gambo, M. Ibrahim, H. U. Hambali and M. Y. Shahul Hamid, A Review on Catalyst Development for Dry Reforming of Methane to Syngas: Recent Advances, *Renewable Sustainable Energy Rev.*, 2019, **108**, 175–193, DOI: **10.1016/J.RSER.2019.03.054**.

38 M. A. Alsaffar, B. V. Ayodele and S. I. Mustapa, Scavenging Carbon Deposition on Alumina Supported Cobalt Catalyst during Renewable Hydrogen-Rich Syngas Production by Methane Dry Reforming Using Artificial Intelligence Modeling Technique, *J. Cleaner Prod.*, 2020, **247**, 119168, DOI: **10.1016/j.jclepro.2019.119168**.

39 S. M. Sidik, S. Triwahyono, A. A. Jalil, Z. A. Majid, N. Salamun, N. B. Talib and T. A. T. Abdullah, CO2 Reforming of CH4 over Ni-Co/MSN for Syngas Production: Role of Co as a Binder and Optimization Using RSM, *Chem. Eng. J.*, 2016, **295**, 1–10, DOI: **10.1016/j.cej.2016.03.041**.